Department of Physics and Astronomy
Heidelberg University

Bachelor Thesis in Physics
submitted by

Moritz Thierfeld

born in Schkeuditz (Germany)

2024

Hadronic vacuum polarization of muonic atoms

This Bachelor Thesis has been carried out by Moritz Thierfeld at the
Max Planck Institute for Nuclear Physics in Heidelberg
under the supervision of
PD Dr. Natalia S. Oreshkina

Abstract

In this Thesis, the shift in atomic energy levels due to hadronic vacuum polarization is assessed using a semiempirical approach for hydrogen-like ions and muonic atoms as well. A parametric hadronic polarization function, derived from experimental data on electron-positron annihilation into hadrons, is used to develop an effective relativistic uehling potential. Energy corrections from hadronic vacuum polarization are computed for low-lying levels using analytical Dirac-Coulomb wave functions, along with wave functions that account for the finite size of the nucleus. The study also derives explicit formulas for the hadronic Uehling potential in the case of an extended nucleus and for the relativistic energy shift in the case of a pointlike nucleus. These results are subsequently compared with existing analytical formulas derived from nonrelativistic theory.

In dieser Arbeit wird die Verschiebung atomarer Energieniveaus aufgrund hadronischer Vakuumpolarisation mit Hilfe eines semiempirischen Ansatzes auch für wasserstoffähnliche Ionen und myonische Atome untersucht. Eine parametrische hadronische Polarisationsfunktion, die aus experimentellen Daten zur Elektron-Positron-Annihilation in Hadronen abgeleitet wurde, dient zur Entwicklung eines effektiven relativistischen Uehling-Potentials. Die Energiekorrekturen durch die hadronische Vakuumpolarisation werden für niedrig liegende Niveaus mit analytischen Dirac-Coulomb-Wellenfunktionen als auch für Wellenfunktionen, welche die endliche Größe des Kerns berücksichtigen berechnet. In der Thesis werden auch explizite Formeln für das hadronische Uehling-Potenzial im Fall eines ausgedehnten Kerns und für die relativistische Energieverschiebung im Fall eines punktförmigen Kerns abgeleitet. Diese Ergebnisse werden anschließend mit bestehenden analytischen Formeln aus der nichtrelativistischen Theorie verglichen.

Table of Contents

1 Introduction

The progress of modern physics is often driven by resolving discrepancies between theoretical predictions and experimental observations. These efforts frequently lead to the development of more advanced theories, known as "new physics." Among these, Quantum Electrodynamics (QED), a fundamental part of the Standard Model, stands out as one of the most precise and thoroughly validated theories. QED provides an exceptionally accurate framework for describing the electromagnetic interactions between charged particles and photons. Its predictions, such as the transition frequencies of atomic hydrogen and the gyromagnetic ratio of the electron, have been confirmed with remarkable precision, making it one of the most rigorously tested theories in physics [1]. Despite its success, as experimental techniques continue to advance, more subtle quantum effects need to be accounted for to preserve this theoretical accuracy. One such effect is vacuum polarization (VP), where virtual particle-antiparticle pairs are momentarily created and annihilated in the vacuum. The most significant contributions to VP come from virtual electron-positron and muon-antimuon pairs, which are relatively well understood [2]. However, a more complex correction arises from hadronic vacuum polarization (HVP), involving virtual quark-antiquark pairs that interact via the strong force. Unlike the simpler electron-based case, calculating hadronic vacuum polarization is significantly more challenging due to the involvement of Quantum Chromodynamics (QCD), the theory governing strong interactions. In this study, we assess the shifts in atomic energy levels caused by hadronic vacuum polarization using a semiempirical approach for both hydrogen-like ions and muonic atoms. Muonic atoms offer unique advantages for studying hadronic vacuum polarization due to the distinctive properties of the muon. Being about 207 times heavier than the electron, the muon orbits much closer to the nucleus in muonic atoms. This proximity significantly enhances the sensitivity of the atom to quantum effects like vacuum polarization and nuclear structure corrections—effects that are far less prominent in electron-based systems, as shown in Fig. 1. Recent advances in

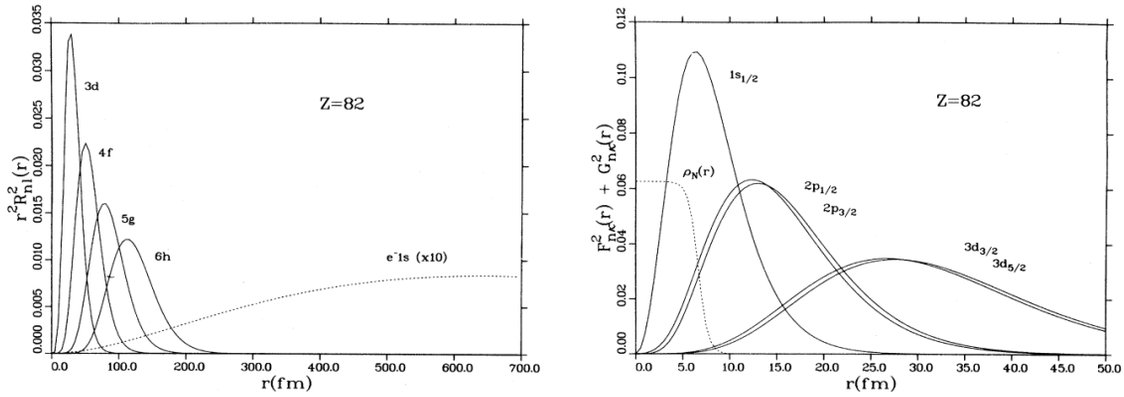

Figure 1: Left: Muon wave functions (solid lines) for relatively high lying states, compared to electron 1s state (dashed line) Right: Muon wave functions (solid lines) for relatively low-lying states, compared to the nuclear charge distribution $\rho_N(r)$ (dashed line). Figure is taken from [2].

precision laser spectroscopy have further improved the accuracy with which energy levels in muonic atoms can be measured [3]. These developments position muonic systems as powerful tools for testing QED and probing hadronic effects with exceptional precision. By employing a semiempirical approach utilizing experimental hadronic data to model the polarization function and applying relativistic wave functions. This semiempirical method allows for a more precise representation of HVP effects, particularly at the energy scales relevant to muonic systems. This study bridges the gap between theoretical predictions and experimental data. In doing so, it contributes to the broader effort to push the boundaries of our understanding of fundamental physics, offering insights into both QED and potential new physics.

2 Notation

In this thesis, we will use natural units where the reduced Planck constant $\hbar$, the speed of light c, and the vacuum permittivity ε_0 are all set to 1: $\hbar = c = \varepsilon_0 = 1$. Within this framework, the fine-structure constant α is given by $\alpha = \frac{e^2}{4\pi}$, where e represents the elementary charge. The standard unit for mass and energy in this system is the electronvolt (eV), with 1 eV being equivalent to 1.602×10^{-19} joules. Throughout this work, we will use the values for physical constants provided by the Committee on Data for Science and Technology (CODATA) [4]:

$$\alpha = \frac{1}{137.035\,999\,084(21)}, \tag{1}$$

$$m_e = 0.510\,998\,950\,00(15)\,\text{MeV}, \tag{2}$$

$$\frac{m_\mu}{m_e} = 206.768\,2830(46). \tag{3}$$

3 Radial Dirac equation

When examining an electron in a central potential field, such as the Coulomb potential generated by a nucleus, the Dirac equation provides a comprehensive framework that incorporates relativistic effects, spin-orbit coupling, and the fine structure of atomic spectra. The radial Dirac equation is a reformulation of the Dirac equation specifically for spherically symmetric potentials. It separates the wave function into angular and radial components, simplifying the problem to a set of coupled differential equations. These equations are fundamental for understanding the behavior of relativistic particles in atomic and nuclear systems.

3.1 Derivation of the Hamiltonian form of the Dirac equation

The time-dependent Dirac equation in natural units (where $\hbar = c = 1$) is given by [5]:

$$i\frac{\partial\psi}{\partial t} = \left(\hat{\beta}m - i\sum_{n=1}^{3}\hat{\alpha_n}\frac{\partial}{\partial x^n}\right)\psi \tag{4}$$

where:

- ψ is a four-component spinor wavefunction that represents the state of a spin-$\frac{1}{2}$ particle.
- $\hat{\alpha}_n$ (for $n = 1, 2, 3$) and $\hat{\beta}$ are 4×4 Hermitian matrices known as the Dirac matrices. They fulfill the following identities to ensure the consistency of the equation with special relativity and incorporate the anticommutation behavior. Here the relation between the well known gamma matricies γ_μ, satisfying the Clifford algebra, is $\hat{\beta} = \gamma_0, \hat{\alpha_i} = \hat{\beta}\gamma_i$

$$\{\hat{\alpha}_i, \hat{\alpha}_j\} = 2\delta_{ij}I, \quad \{\hat{\alpha}_i, \hat{\beta}\} = 0, \quad \hat{\beta}^2 = I,$$

- The Dirac matrices α_i and β used in this formulation are given by:

$$\alpha_i = \begin{pmatrix} 0 & \sigma_i \\ \sigma_i & 0 \end{pmatrix}, \quad \beta = \begin{pmatrix} \mathbb{I}_{2\times2} & 0 \\ 0 & -\mathbb{I}_{2\times2} \end{pmatrix} \tag{5}$$

  where I is the identity matrix and δ_{ij} is the Kronecker delta.

To express the Dirac equation in Hamiltonian form, we introduce the momentum operator $\hat{p}_i = -i\frac{\partial}{\partial x^i}$. Substituting this into the equation, we can rewrite it as:

$$i\frac{\partial\psi}{\partial t} = \left(\hat{\beta}m + \sum_{n=1}^{3}\hat{\alpha}_i\hat{p}_i\right)\psi. \tag{6}$$

The expression within the parentheses defines the Dirac Hamiltonian operator $\hat{H}_D$:

$$\hat{H}_D = \hat{\beta}m + \sum_{n=1}^{3}\hat{\alpha}_i\hat{p}_i. \tag{7}$$

Thus, the Dirac equation in Hamiltonian form can be compactly written as:

$$i\frac{d\psi}{dt} = \hat{H}_D\psi. \tag{8}$$

3.2 Electron in a central potential V(r)

The Dirac Hamiltonian for an electron in a spherically symmetric potential $V(r)$ is expressed as

$$\hat{H}_D = \sum_{n=1}^{3}\hat{\alpha}_i\hat{p}_i + \hat{\beta}m_e + V(r), \tag{9}$$

where $\hat{p}_i$ represents the momentum operator, $\hat{\alpha}_i$ and $\hat{\beta}$ are the Dirac matrices, and m_e is the mass of the electron. Given the spherical symmetry of the potential $V(r)$, the operators for parity and angular momentum commute with the Hamiltonian. As a result, the system's eigenstates can be labeled by their energy, total angular momentum j, orbital angular momentum l, and parity. These eigenstates can be represented as a 4-component spinor ψ_{jlm}, which can be decomposed into two 2-spinors due to the symmetry of the problem [5]:

$$\psi_{jlm}(\vec{r}) = \begin{pmatrix} \varphi_{jlm}(\vec{r}) \\ \chi_{jl'm}(\vec{r}) \end{pmatrix} = \begin{pmatrix} ig(r)\Omega_{jlm}(\hat{r}) \\ -f(r)\Omega_{jl'm}(\hat{r}) \end{pmatrix}, \tag{10}$$

where $\Omega_{jlm}(\hat{r})$ is the spherical spinor, which is an eigenfunction of the total angular momentum and parity operators, and $\hat{r} = \vec{r}/r$ is the unit vector in the direction of $\vec{r}$. Here, $l' = 2j - l$ is chosen to ensure that the large and small components of the spinor ψ_{jlm} have opposite parity. The spherical spinor Ω_{jlm} satisfies the following identity:

$$\left(\sum_{n=1}^{3} \sigma_i r_i\right) \frac{\Omega_{jlm}}{r} = -\Omega_{jl'm} \tag{11}$$

where σ_i are the Pauli matrices, and the sum runs over the spatial coordinates $i = 1, 2, 3$. Here $\mathbb{I}_{2\times 2}$ is the 2×2 identity matrix. In this notation the stationary Dirac equation becomes [5]:

$$\begin{aligned} (E - m - V(r))\varphi_{jlm} &= \left(\sum_{n=1}^{3} \sigma_i \hat{p}_i\right) \chi_{jl'm}, \\ (E + m - V(r))\chi_{jl'm} &= \left(\sum_{n=1}^{3} \sigma_i \hat{p}_i\right) \varphi_{jlm}. \end{aligned} \tag{12}$$

Those expressions can be rewritten making use of the spherical spinors and the identity just shown which results in:

$$\begin{aligned} \left(\sum_{n=1}^{3} \sigma_i \hat{p}_i\right) \varphi_{jlm} &= \frac{dg(r)}{dr} \left(\sum_{n=1}^{3} \sigma_i r_i\right) \frac{\Omega_{jlm}}{r} + ig(r) \left(\sum_{n=1}^{3} \sigma_i \hat{p}_i\right) \Omega_{jlm} \\ &= -\frac{dg(r)}{dr} \Omega_{jl'm} - g(r) \left(\frac{2}{r} + \frac{1}{r} \left(\sum_{n=1}^{3} \hat{L}_i \sigma_i\right)\right) \Omega_{jl'm}. \end{aligned} \tag{13}$$

Introducing a new operator $\hat{\kappa}$ with the sperical spinors as eigenfunctions:

$$\hat{\kappa} = 1 + \left(\sum_{n=1}^{3} \hat{L}_i \sigma_i\right) \; with \; \hat{\kappa}\chi_{km} = -\kappa\chi_{km}, \tag{14}$$

$$\text{and } \kappa = \begin{cases} -\left(j+\frac{1}{2}\right) = -(l+1), & \text{for } j = l+\frac{1}{2}, \\ +\left(j+\frac{1}{2}\right) = l, & \text{for } j = l-\frac{1}{2}. \end{cases} \tag{15}$$

Thus, for Eq. (13) and through a similar calculation for the other spinor component, we obtain:

$$\left(\sum_{n=1}^{3} \hat{\sigma}_i \hat{p}_i\right) \varphi_{jlm} = -\Omega_{jlm} \left(\frac{dg(r)}{dr} + \frac{\kappa+1}{r} g(r)\right), \tag{16}$$

$$\left(\sum_{n=1}^{3} \hat{\sigma}_i \hat{p}_i\right) \chi_{jlm} = -i\Omega_{jlm} \left(\frac{df(r)}{dr} - \frac{\kappa-1}{r} f(r)\right). \tag{17}$$

By substituting these expressions into Eq. (13), the spinors cancel out. The resulting differential equations for the radial functions are:

$$\frac{dg(r)}{dr} + \frac{(1+\kappa)g(r)}{r} - (E + m - V(r))\, f(r) = 0, \tag{18}$$

$$\frac{df(r)}{dr} + \frac{(1-\kappa)f(r)}{r} - (E - m - V(r))\, g(r) = 0. \tag{19}$$

Defining $G(r) \equiv rg(r)$ and $F(r) \equiv rf(r)$ we obtain the well known form of the coupled differential equations [5]:

$$\frac{dG(r)}{dr} + G(r)\frac{\kappa}{r} - (E + m - V(r))\, F(r) = 0, \tag{20}$$

$$\frac{dF(r)}{dr} - F(r)\frac{\kappa}{r} - (E - m - V(r))\, G(r) = 0. \tag{21}$$

Which can also be brought into matrix form which is given like this for an electron with mass m_e:

$$\begin{pmatrix} V(r) + m_e & \frac{\kappa}{r} - \frac{d}{dr} \\ \frac{\kappa}{r} + \frac{d}{dr} & V(r) - m_e \end{pmatrix} \begin{pmatrix} G(r) \\ F(r) \end{pmatrix} = E \begin{pmatrix} G(r) \\ F(r) \end{pmatrix}. \tag{22}$$

The radial Dirac equation governs the wave functions and energy levels of relativistic electrons within atoms. The spectrum of this equation includes both bound states, characterized by discrete energy eigenvalues, and continuum states, with eigenvalues ranging over the intervals $(-\infty, m_e]$ and $[m_e, +\infty)$. The bound-state solutions correspond to normalizable wavefunctions with discrete energy eigenvalues, denoted as E. These bound-state

wavefunctions can be expressed as [6]:

$$\psi_{n\kappa m}(r) = \frac{1}{r}\begin{pmatrix} G_{n\kappa}(r)\Omega_{\kappa m}(n) \\ iF_{n\kappa}(r)\Omega_{-\kappa m}(n) \end{pmatrix}, \tag{23}$$

Continuum solutions, which are associated with the continuous spectrum, are instead labeled by a real-valued eigenvalue rather than the principal quantum number n. While for a point like nucleus with $V(r) = -Z\alpha/r$ the bound state and continious solutions can be given analytically, for the treatment of extended nuclei the radial Dirac equation needs to be solved numerically [7].

4 Leptonic vacuum polarization effect

Vacuum polarization is a quantum electrodynamic (QED) effect in which the vacuum, traditionally considered an empty void, exhibits complex behavior due to the transient existence of virtual particle-antiparticle pairs, such as electron-positron pairs. These virtual pairs spontaneously emerge from the quantum vacuum as a consequence of inherent quantum fluctuations, in accordance with the Heisenberg uncertainty principle. These effects can be categorized into 3 groups shown in Fig. 2

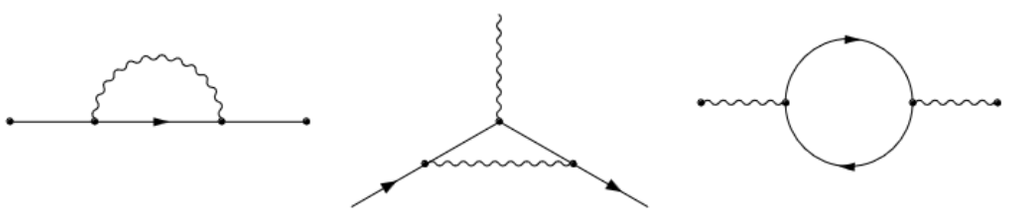

(a) Self-energy correction (b) Vertex correction (c) Virtual e^+/e^--pair production

Figure 2: QED corrections to the free electron propagator (straight arrow line) and the free photon propagator (wave line).Picture is taken from [8].

When an external electromagnetic field is present, these virtual particles interact with the field, resulting in a temporary polarization of the vacuum. This phenomenon is analogous to the behavior of a dielectric material in a conventional electromagnetic field, where the virtual pairs orient themselves in such a way that their charges partially screen the external field. As a result, vacuum polarization induces several significant effects. One of the primary effects is the screening of a particle's charge by the virtual particle-antiparticle pairs generated in the vacuum, effectively altering the perceived or "effective" charge of the particle. This screening effect leads to a scale-dependent charge: at shorter distances (or higher energies), the particle appears to have a higher charge because the virtual pairs are less effective at screening it. Conversely, at larger distances, the effective charge is reduced due to the more significant screening effect of the virtual pairs. Vacuum polarization causes α, the fundamental constant that determines the strength of electromagnetic

interactions, to become energy-dependent. As the energy scale increases, the virtual pairs in the vacuum become less efficient at screening the particle's charge. Consequently, the effective charge observed at higher energies increases, leading to an increase in the value of the fine-structure constant. This variation of α with the energy scale is known as the "running" of the fine-structure constant, reflecting how electromagnetic interactions become stronger at shorter distances or higher energies [5]. In formal QED treatments, vacuum polarization effects are often handled by modifying the photon propagator, $D_{\mu\nu}(q)$, to account for the interaction of the photon with virtual charged particles. This modification can be expressed in terms of the vacuum polarization tensor, $\Pi_{\mu\nu}(q)$. The vacuum polarization tensor encapsulates the correction to the photon propagator resulting from the creation and annihilation of virtual particle-antiparticle pairs in the vacuum. It is through this modification that one can accurately describe how the photon propagates in a vacuum that is "polarized" by these quantum fluctuations, leading to observable phenomena such as the scale dependence of the fine-structure constant and charge screening effects [9].

$$iD^{mod}_{\mu\nu}(q) = iD_{\mu\nu}(q) + iD_{\mu\lambda}(q)\frac{i\Pi^{\lambda\sigma(q)}}{4\pi}D_{\sigma\nu}(q), \tag{24}$$

$$\Pi_{\lambda\sigma}(q) = (q^2\eta_{\lambda\sigma} - q_\lambda q_\sigma)\Pi(q^2). \tag{25}$$

Here $\Pi(q^2)$ denotes the divergent polarization function and $\eta_{\mu\nu} = diag(1, -1, -1, -1)$ was used. Therefore after correctly regularizing and renormalising the polarisation function only the real part $Re[\Pi^R(q^2)]$ takes part in actual calculations. The vacuum polarization hence can be described by an static effective potential called the Uehling potential, describing one of the most important corrections to the Coulomb law. It is given like [9]:

$$\delta V(\mathbf{x}) = \int \frac{d^3q}{(2\pi)^3} e^{i\mathbf{qx}} \left(\frac{-4\pi e}{\mathbf{q}^2}\right) \tilde{\rho}(\mathbf{q}) Re[\Pi^R(-\mathbf{q}^2)] \tag{26}$$

This contribution can be addressed solely through perturbation theory. Alternatively, it also can be incorporated as an electrostatic potential when solving the Dirac equation. Formally, one computes the scattering amplitude from Feynman diagrams and seeks an effective potential that reproduces the correct first-order Born approximation for the scattering amplitude. Using this so-called Uehling potential, the first-order energy shifts can then be determined.

5 Hadronic vacuum polarization

The leptonic polarization function can be calculated analytically, either as an expansion in powers of the nuclear coupling strength $Z\alpha$ or, in some cases, even exactly, as shown above. In contrast, calculating the hadronic vacuum polarization (VP) shift is more challenging because the produced particles interact strongly, making perturbative quantum

chromodynamic approaches ineffective. Feynman diagrams contributing to this effect are shown schematic in Fig. 3. Therefore, a semi-empirical approach is used to construct the

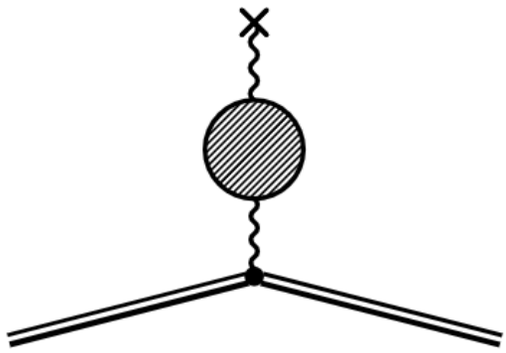

Figure 3: Leading Hadronic vacuum polarization contribution depicted as Feynman diagram. Here the double line represents the bounded electron interacting with the coulomb field shown by the cross. The wave line with the shaded area in between depicts the modified photon propagator duo to hadronic VP. Picture is taken from [10].

real part of the renormalized and regularized hadronic polarization function, $Re[\Pi^R_{\text{had}}(q^2)]$. In the following, we will introduce the method for constructing the real part of the renormalized and regularized hadronic polarization function, $Re[\Pi^R_{\text{had}}(q^2)]$, from experimental $e^+e^- \to$ hadrons collision data [11]. To proceed with the analysis, it is essential to introduce two fundamental concepts in theoretical physics: the Kramers-Kronig relation and the optical theorem. These concepts are critical for understanding the connection between measurable quantities and underlying theoretical constructs.

5.1 Kramers-Kronig relation

The Kramers-Kronig relation is a powerful tool in complex analysis, particularly in the context of response functions in quantum field theory. It provides a rigorous way to relate the real and imaginary parts of a complex function, such as the polarization function, by leveraging the principle of causality. Specifically, the real part of the function, which corresponds to dispersive effects, can be derived from its imaginary part, associated with absorptive processes, and vice versa. This relationship is integral in the calculation of the vacuum polarization (VP) effects, as it allows the determination of the full polarization function from experimental data. Using the desired vacuum polarization function we find the following relation. Where $\mathcal{P}\int_a^b dx$ is the principal value integral:

$$Re[H(x)] = \frac{1}{\pi}\mathcal{P}\int_{-\infty}^{\infty} \frac{Im[H(x')]}{x'-x}dx'. \tag{27}$$

In the case of hadronic scattering the Kramers-Kronig relation is also known as the "integral dispersion relation" where here the function to be considered is the scattering amplitude [8].

$$Re[\Pi^R(q^2))] = \frac{q^2}{\pi}\mathcal{P}\int_{-\infty}^{\infty}\frac{Im[\Pi^R(q'^2)]}{q'^2(q'^2 - q^2 - i\epsilon)}dq'^2. \tag{28}$$

5.2 Optical theorem

The optical theorem is a cornerstone of quantum scattering theory, providing a deep connection between the total cross-section of a scattering process and the imaginary part of the forward scattering amplitude. The theorem emerges from the unitarity of the S-matrix, a fundamental concept that ensures the conservation of probability in quantum mechanical processes. The S-matrix encapsulates the entire scattering process, relating the initial and final states, and its unitarity guarantees that the sum of probabilities of all possible outcomes equals one. Mathematically, the optical theorem can be expressed as:

$$\sigma_{tot} = \frac{4\pi}{|k|}Imf[(k,0)], \tag{29}$$

where σ_{tot} is the total cross-section, k is the magnitude of the incident particle's momentum, and $f(k,0)$ is the forward scattering amplitude (i.e., the scattering amplitude at zero scattering angle). The imaginary part of the forward scattering amplitude, $Im[f(k,0)]$, is directly related to the absorptive processes, which correspond to the loss of flux due to scattering into any possible final states. To conclude the optical theorem implies that the amplitude for an initial state transitioning into any final state is proportional to twice the imaginary part of the forward scattering amplitude for the process where the initial and final states are identical, but with any possible intermediate states involved. In essence, it quantifies the probability for the total scattering process by relating it to the imaginary component of the amplitude associated with the initial state scattering forward into itself. For the specific case of electron-positron annihilation into hadronic matter, the optical theorem can be expressed as [11]:

$$\sigma_{tot}(e^+e^- \to hadrons; q^2) = \frac{4\pi\alpha}{q^2}Im[\Pi^R_{had}]. \tag{30}$$

In an experiment, measuring a total cross-section on the absolute scale can be challenging due to various experimental uncertainties and the need for precise calibration. To overcome this difficulty, it is common to use a relative measure of the total cross-section, denoted as $R(q^2)$. This relative cross-section is typically defined in relation to the well-understood and more easily measurable process of muon pair creation in electron-positron annihilation. The quantity $R(q^2)$ is defined as:

$$R(q^2) = \frac{\sigma_{tot}(e^+e^- \to hadrons; q^2)}{\sigma_{tot}(e^+e^- \to \mu^+\mu^-; q^2)}, \tag{31}$$

where $\sigma_{tot}(e^+e^- \to hadrons; q^2)$ is the total cross-section for the production of hadrons in electron-positron annihilation at a given squared center-of-mass energy q^2 and $\sigma_{tot}(e^+e^- \to$

$\mu^+\mu^-; q^2)$ is the total cross-section for the production of a muon-antimuon pair at the same energy q^2. By using this relative measure, experimentalists can bypass some of the complexities associated with absolute cross-section measurements. The ratio $R(q^2)$ has the advantage of canceling out many systematic uncertainties, such as those related to luminosity measurements or detection efficiencies, which affect both the hadronic and muonic processes similarly. Moreover, the cross-section for muon pair production is well-predicted by quantum electrodynamics (QED) and serves as a reliable reference. This ratio $R(q^2)$ is particularly important in constructing the hadronic vacuum polarization function because it encapsulates the energy dependence of the hadronic cross-section relative to a known benchmark. The data for $R(q^2)$ across different energies can then be used to refine theoretical model. In the follwoing we briefly reproduce the calculation of the muon pair production cross section which is known very well.

5.3 Brief revision of muon pair production cross section

In this Chapter we briefly discuss and summerize the main steps to calculate the muon pair production cross section. Following [12] we find for the $2 \to 2$ Lorentz-invariant differential cross section $d\sigma$:

$$d\sigma = \frac{(2\pi)^4}{4E_p E_{p'} |\vec{\nu}_p - \vec{\nu}_{p'}|} \frac{d^3k}{(2\pi)^3 2E_k} \frac{d^3k'}{(2\pi)^3 2E_{k'}} \delta^(4)(p + p' - k - k')|M_{fi}|^2. \tag{32}$$

The momenta p, p' and energies $E_p, E_{p'}$ of the incoming particles, the momenta k, k' and energies $E_k, E_{k'}$ of the outgoing particles, and the ratio of the 3-momentum to the energy of a particle $\vec{\nu}_p = \vec{p}/E_p$. The invariant matrix element iM of the $\sigma_{\text{tot}}(e^+e^- \to \mu^+\mu^-; q^2)$ process using Feynman rules is given by:

$$iM(q^2) = \frac{ie^2}{q^2} \bar{v}_{s'}(p')\gamma^\mu u_s(p)\bar{u}_r(K)\gamma_\mu v_{r'}(k'). \tag{33}$$

When the primary interest is in the q^2-dependence of the cross-section, the detailed information on the polarization of the particles involved becomes less relevant. In this case, the amplitude squared is averaged over the polarization states of both the incoming and outgoing particles. This simplification is achieved by employing the spinor completeness relations, which allow the expression for the cross-section to be written in a more manageable form. For a process like electron-positron annihilation into hadrons, the cross-section can be expressed as:

$$\sigma(q^2) \propto \frac{1}{4} \sum_{\text{spins}} |M|^2, \tag{34}$$

where:

- M is the matrix element (amplitude) for the process,

- The factor $\frac{1}{4}$ accounts for averaging over the initial spin states of the electron and positron (each with two possible spin states), and
- The sum over spins $\sum_{\text{spins}}$ indicates that we sum over all possible spin states of the outgoing particles.

Using the spinor completeness relations, which are fundamental identities in quantum field theory, the spin-averaged matrix element squared can be simplified. The spinor completeness relation for a Dirac spinor $u(p)$ with momentum p and mass m is given by:

$$\sum_{\text{spins}} u(p)\bar{u}(p) = \not{p} + m \tag{35}$$

and for the corresponding antiparticle spinor $v(p)$, it is:

$$\sum_{\text{spins}} v(p)\bar{v}(p) = \not{p} - m \tag{36}$$

, where $\not{p}$ denotes the Feynman slash notation, $\not{p} = \gamma^\mu p_\mu$, with γ^μ being the gamma matrices. These relations are used to replace the spinor products in the matrix element $|M|^2$ with traces over gamma matrices and momentum vectors. As a result, the expression for the cross-section becomes a trace over these objects, which is typically easier to compute:

$$\sigma(q^2) \propto \text{Tr}\left[(\not{p}_1 + m_1)\Gamma(\not{p}_2 + m_2)\Gamma^\dagger\right], \tag{37}$$

where Γ represents the interaction vertex structure (such as γ^μ for QED processes). This trace calculation yields a result that only depends on the kinematic variables, such as the center-of-mass energy q^2, and not on the specific polarization states, thereby focusing solely on the q^2-dependence of the cross-section. This simplification is crucial for studying the energy dependence of the process, which is the main focus when constructing quantities like $R(q^2)$ in hadronic vacuum polarization studies. For our process to consider within the centre of mass frame (cms) we arrive at the follwoing expression for the unpolarized amplitude square $\frac{1}{4}\sum_{\text{spins}} |M|^2$:

$$\frac{1}{4}\sum_{\text{spins}} |\mathcal{M}|^2 = e^4\left[\left(1 + \frac{4m_\mu^2}{q^2} + \frac{4m_e^2}{q^2}\right) + \left(1 - \frac{4m_\mu^2}{q^2} - \frac{4m_e^2}{q^2} + \frac{16m_e^2 m_\mu^2}{q^4}\right)\cos^2\theta\right]. \tag{38}$$

The final result for the total cross section of the $e^+e^- \to \mu^+\mu^-$ process is then:

$$\sigma_{tot}(e^+e^- \to \mu^+\mu^-; q^2) = \frac{4\pi\alpha^2}{3q^2}\frac{\sqrt{1 - \frac{4m_\mu^2}{q^2}}}{\sqrt{1 - \frac{4m_e^2}{q^2}}}\left[\left(1 + \frac{2m_\mu^2}{q^2}\right)\left(1 + \frac{2m_e^2}{q^2}\right)\right]. \tag{39}$$

In the limit where m_e is neglected and $|\vec{p}| \gg m_\mu$ (ultra relativistic limit) this expression

simplifies a lot with the result:

$$\sigma_{tot}(e^+e^- \to hadrons; q^2) = \frac{4\pi\alpha^2}{3q^2}. \tag{40}$$

5.4 Reconstruction of the hadronic polarization function

The real part of the hadronic polarization function $\Pi^R_{\text{had}}(q^2)$ can be linked to its imaginary part making use of the Kramer-Kronig relations. It is given by the following dispersion relation:

$$Re[\Pi^R_{\text{had}}(q^2)] = \frac{q^2}{\pi}\mathcal{P}\int_{-\infty}^{+\infty} \frac{Im[\Pi^R_{\text{had}}(q'^2)]}{q'^2(q'^2 - q^2 - i\epsilon)}dq'^2, \tag{41}$$

where:

- q^2 is the squared momentum transfer of the virtual photon,
- $Im[\Pi^R_{\text{had}}(q'^2)]$ is the imaginary part of the hadronic polarization function.

The imaginary part of the hadronic polarization function $Im[\Pi^R_{\text{had}}(q'^2)]$ then can be expressed in terms of the experimentally measurable cross section for $e^+e^- \to$ hadrons using the optical theorem. The relation is given by:

$$Re[\Pi^R_{\text{had}}(q^2)] = \frac{q^2}{4\pi^2\alpha}\mathcal{P}\int_{4m_\pi^2}^{\infty} \frac{\sigma_{tot}(e^+e^- \to hadrons; q^2)}{q'^2(q'^2 - q^2 - i\epsilon)}dq'^2, \tag{42}$$

where:

- $4m_\pi^2$ represents the threshold for hadron production (with m_π being the mass of the pion, the lightest hadron).

Substituting in the relative cross section $R(q'^2)$, the real part of the hadronic polarization function becomes:

$$Re[\Pi^R_{\text{had}}(q^2)] = \frac{\alpha q^2}{3\pi}\mathcal{P}\int_{4m_\pi^2}^{\infty} \frac{R(q'^2)}{q'^2(q'^2 - q^2 - i\epsilon)}dq'^2. \tag{43}$$

- **Principal Value**: The Cauchy principal value $\mathcal{P}$ ensures that the integral is properly handled around the singularity at $q'^2 = q^2$, where the denominator vanishes.

Thus, the real part of the hadronic polarization function $\Pi^R_{\text{had}}(q^2)$ is constructed from the total hadronic cross section, described by $R(q'^2)$, using this dispersion relation. This relation connects the theoretical description of QCD contributions to the vacuum polarization with experimentally measurable quantities.

6 Approximate parametrization of the hadronic polarization function

The hadronic polarization function can be constructed using experimental collision data, as discussed in detail in the last chapter. This method was implemented, for example, by Burkhardt et al., who compiled data from different experiments across various energy regions. They provided an approximate parameterization for the real part of the polarization function, $Re[\Pi_{\text{had}}(q^2)]$, which is given by [11]:

$$Re[\Pi_{\text{had}}(q^2)] = A_i + B_i \ln\left(1 + C_i \left|q^2\right|\right) \tag{44}$$

where:

- A_i, B_i, and C_i are constants specific to different regions of q^2

Table 1: Values for the parametrization of the hadronic polarization function as given in [13], with the mass of the Z boson m_Z.

Region	Range (GeV)	A_i	B_i	C_i (GeV^{-2})
$k_0 - k_1$	$0.0 - 0.7$	0.0	0.0023092	3.9925370
$k_1 - k_2$	$0.7 - 2.0$	0.0	0.0022333	4.2191779
$k_2 - k_3$	$2.0 - 4.0$	0.0	0.0024402	3.2496684
$k_3 - k_4$	$4.0 - 10.0$	0.0	0.0027340	2.0995092
$k_4 - k_5$	$10.0 - m_Z$	0.0010485	0.0029431	1.0
$k_5 - k_6$	$m_Z - 10^4$	0.0012234	0.0029237	1.0
$k_6 - k_7$	$10^4 - 10^5$	0.0016894	0.0028984	1.0

The Uehling potential for this parameterization, is therefore given by:

$$\delta V_{fns}^{full}(\vec{x}) = -Ze \sum_{i=1}^{7} \left[\int_{k_{i-1}}^{k_i} \frac{d^3q}{(2\pi)^3} e^{i\vec{q}\cdot\vec{x}} \frac{4\pi}{\vec{q}^2} \tilde{\rho}(\vec{q}) \left[A_i + B_i \ln(1 + C_i |\vec{q}|^2) \right] \right] \tag{45}$$

where $\tilde{\rho}(\vec{q})$ denotes the Fourier transform of the charge distribution. For a spherically symmetric charge distribution $\tilde{\rho}(\vec{q})$, the angular integrations can be simplified by employing spherical coordinates, yielding:

$$\delta V_{fns}^{full}(r) = -Ze \frac{2}{\pi} \sum_{i=1}^{7} \int_{k_{i-1}}^{k_i} dq |q| j_0(|q|r) \left[A_i + B_i \ln(1 + C_i |q|^2) \right] \tilde{\rho}(|q|), \tag{46}$$

where $r = |\vec{r}|$, $|q| = |\vec{q}|$, and $j_0(x) = \frac{\sin(x)}{x}$ is the spherical Bessel function of the first kind. The function $j_0(x)$ accounts for the angular dependence, and the resulting expression explicitly shows the relationship between the Uehling potential and the radial distance r. For the sake of calculating energy shifts of low lying states, later on a reliable approximation of the full polarization function can be obtained by focusing on the parameters from

its first momentum region extending to infinity, specifically using A_1, B_1, and C_1. In this framework, the Uehling potential for a pointlike nucleus, where $\tilde{\rho}(\vec{q}) = Ze$, reduces to:

$$\delta V_{\text{point}}^{\text{approx}}(r) = -\frac{2Z\alpha}{\pi} \int_0^\infty dq\, j_0(qr) \left[B_1 \ln(1 + C_1 q^2)\right], \tag{47}$$

which simplifies to:

$$\delta V_{\text{point}}^{\text{approx}}(r) = -\frac{2Z\alpha}{r} B_1 E_1 \left(\frac{r}{\sqrt{C_1}}\right), \tag{48}$$

where the exponential integral $E_n(x)$ is given by:

$$E_n(x) = \int_1^\infty \frac{e^{-xt}}{t^n} dt. \tag{49}$$

This approximation is well-justified on physical grounds, as the low-energy region is of paramount importance in atomic physics. Moreover, the original parameterization, applicable up to 0.7 GeV, is sufficiently accurate for our intended applications [10].

6.1 Finite nuclear size effects

The study of the muonic vacuum polarization (VP) is critically influenced by finite nuclear size effects, an aspect that becomes even more pronounced when considering hadronic contributions. The hadronic Uehling potential, in particular, presents significant computational challenges, especially when compared to its leptonic counterpart. Given the complexity and computational demands associated with the numerical integration required for the hadronic Uehling potential, it becomes imperative to adopt a simplified yet effective model of the nuclear charge distribution.

6.2 Model of the nucleus as a homogeneously charged sphere

In this context, a homogeneously charged sphere is employed as a model for the nucleus. This model assumes a uniform charge distribution within a sphere of radius R, beyond which the charge density drops to zero. The charge density $\rho(x)$ can be mathematically described as follows:

$$\rho(x) = \begin{cases} \dfrac{3Ze}{4\pi R^3}\theta(R - x), & \text{for } x \leq R, \\ 0, & \text{for } x > R, \end{cases} \tag{50}$$

where x denotes the radial distance from the nucleus's center, and R being related to the root-mean-square (rms) nucelar radius via:

$$R = \sqrt{\frac{5}{3}\langle r^2 \rangle}. \tag{51}$$

The Fourier transform of the charge density, $\tilde{\rho}(q)$, is instrumental in transitioning from position space to momentum space, thereby facilitating the analysis of the Uehling potential. For the homogeneously charged sphere, the Fourier transform is derived as:

$$\tilde{\rho}(q) = 3\left(\frac{\sin(qR) - qR\cos(qR)}{q^3R^3}\right), \tag{52}$$

where q is the radial part of $\vec{q}$. This expression can be further simplified by recognizing the presence of the spherical Bessel function $j_1(x)$, leading to the more compact form:

$$\tilde{\rho}(|q|) = Ze\frac{3j_1(|q|R)}{|q|R}, \tag{53}$$

where $j_1(x)$ is defined as:

$$j_1(x) = \frac{\sin(x)}{x^2} - \frac{\cos(x)}{x}. \tag{54}$$

The finite size of the nucleus has a significant impact on the Uehling potential, particularly in muonic atoms, where the muon orbits much closer to the nucleus compared to an electron. By incorporating a finite nuclear radius R, the divergence of the Uehling potential at the origin (i.e., at $q = 0$) is effectively mitigated.

6.3 Convolution of the charge distribution $\rho(\vec{x})$

Another way of implementing the Uehling potential corresponding to a finite-size nucleus can be obtained by performing a convolution of the Uehling potential for a pointlike nucleus with the charge distribution $\rho(\vec{x})$ of the nucleus in real space. This method allows for the incorporation of finite-size effects into the Uehling potential, which is crucial for accurately modeling the electromagnetic interactions in systems where the finite nuclear size cannot be neglected. The finite-size Uehling potential, denoted as $\delta V_{\text{fns}}^{\text{approx}}(r)$, is expressed as [10]:

$$\delta V_{\text{fns}}^{\text{approx}}(\vec{r}) = \frac{1}{Ze}\int d^3x\, \rho(\vec{x})\delta V_{\text{point}}^{\text{approx}}(\vec{r} - \vec{x}), \tag{55}$$

where $\delta V_{\text{point}}^{\text{approx}}(\vec{r}-\vec{x})$ represents the Uehling potential for a pointlike nucleus evaluated at the position $\vec{r}-\vec{x}$, and Ze is the total charge of the nucleus. This convolution integrates the pointlike potential over the entire volume of the nucleus, weighted by the charge density $\rho(x)$, thus accounting for the spatial distribution of the nuclear charge. To simplify the evaluation of this potential, one can substitute the approximated Uehling potential for a pointlike nucleus $\delta V_{\text{point}}^{\text{approx}}(r)$ and assume a spherically symmetric charge distribution. This assumption significantly reduces the complexity of the convolution integral, leading to the following expression for the finite-size Uehling potential:

$$\delta V_{\text{fns}}^{\text{approx}}(r) = -\frac{4\pi eB_1\sqrt{C_1}}{r}\int_0^\infty dx\, x\rho(x)D_2(r,x), \tag{56}$$

where $D_2(r,x)$ is a function that captures the dependence of the potential on the radial positions r and x, and is defined as:

$$D_n^{\pm}(r,x) = E_n\left(\frac{|r-x|}{\sqrt{C_1}}\right) \pm E_n\left(\frac{r+x}{\sqrt{C_1}}\right), \tag{57}$$

with C_1 being the constant of the parametrized hadronic Uehling potential given in Table 1. $E_n(x)$ is defined as:

$$E_n(x) = \int_1^{\infty} \frac{e^{-xt}}{t^n}\, dt, \tag{58}$$

where n is a positive integer and x is a real number. For the homogeneously charged model, the integral can be solved analytically by dividing it into two distinct solutions: one for the region outside the nucleus and another for the region inside the nucleus:

$r > R$:

$$\delta V_{\text{fns,out}}^{\text{approx}}(r) = -\frac{3Z\alpha B_1\sqrt{C_1}}{rR^3} \times \left\{\sqrt{C_1}RD_3^{+}(r,R) - C_1 D_4^{-}(r,R)\right\}, \tag{59}$$

$r \leq R$:

$$\begin{aligned}\delta V_{\text{fns,in}}^{\text{approx}}(r) = -\frac{3Z\alpha B_1\sqrt{C_1}}{rR^3} \times \Bigg\{ & \sqrt{C_1}T + \sqrt{C_1}RE_3\left(\frac{r+R}{\sqrt{C_1}}\right) + C_1E_4\left(\frac{r+R}{\sqrt{C_1}}\right) \\ & -\frac{1}{6}e^{-\frac{r}{\sqrt{C_1}}}\left[2C_1 + \sqrt{C_1}(r+2R) + (r-R)(r+2R)\right] \\ & -\frac{(r-R)^2(r+2R)}{6\sqrt{C_1}}E_1\left(\frac{R-r}{\sqrt{C_1}}\right)\Bigg\}. \end{aligned} \tag{60}$$

7 Numerical methods

7.1 Finite basis representation

The radial Dirac equation given in Eq. (4) can be written in the form

$$H_\kappa \phi = E\phi, \tag{61}$$

where

$$H_\kappa = \begin{pmatrix} V(r) + m_e & \dfrac{\kappa}{r} - \dfrac{d}{dr} \\ \dfrac{\kappa}{r} + \dfrac{d}{dr} & V(r) - m_e \end{pmatrix}, \tag{62}$$

and ϕ is the vector of radial functions

$$\phi(r) = \begin{pmatrix} G(r) \\ F(r) \end{pmatrix}. \tag{63}$$

Here for any ϕ_1 and ϕ_2 of such vectors not necessarily satisfying the radial Dirac equation, we define the scalar product like this:

$$\langle \phi_1 | \phi_2 \rangle = \int_0^\infty dr \, \left[G_1(r) G_2(r) + F_1(r) F_2(r) \right]. \tag{64}$$

The radial Dirac equation can be derived by varying the action

$$S(\phi) = \langle \phi | H_k | \phi \rangle - E \langle \phi | \phi \rangle, \tag{65}$$

where proper boundary conditions are applied to the components G and F. In this scenario, the system is confined within a spherical cavity of radius R_{cav}, with boundary conditions set at $r = 0$ and $r = R_{\text{cav}}$. This restriction to a finite cavity is the reason that the continuous part of the spectrum becomes discrete. Practically, R_{cav} is chosen to be sufficiently large so that the results are unaffected by the specific choice of radius. The objective is to approximate the radial wave functions using a finite set of basis functions [6]. This converts the radial Dirac equation, which is an ordinary differential equation, into an algebraic equation with a numerically generated spectrum of finite size. This computed spectrum and the corresponding functions are then utilized to compute spectral sums. The function ϕ is approximated using a finite linear combination:

$$\phi(r) = \sum_{i=1}^{2N} c_i u_i(r), \tag{66}$$

where c_i are coefficients and $u_i(r)$ are basis functions. The u_i are assumed to be basis functions of a suitable space of functions chosen to approximate the radial wave functions and which satisfy proper boundary conditions. Using this finite basis set representation for the wavefunctions above we obtain a multivaried function of the coefficients c_i for our action. Since physical wave functions, which are solutions that satisfy the radial Dirac equation, are stationary points of the action, this is equivalent to finding the set of coefficients for which the derivative of S with respect to these coefficients vanishes. This results in a generalized eigenvalue equation for the vector $\mathbf{c}$ of coefficients $c_1, \ldots, c_{2N}$, given by

$$A \cdot \mathbf{c} = \epsilon \, B \cdot \mathbf{c}, \tag{67}$$

where the components of the symmetric $2N \times 2N$ matrices A and B are defined as

$$A_{ij} = \frac{\langle u_i | H_\kappa | u_j \rangle + \langle u_j | H_\kappa | u_i \rangle}{2}, \tag{68}$$

and

$$B_{ij} = \langle u_i | u_j \rangle. \tag{69}$$

By solving the generalized eigenvalue equation in Eq. (67) for a given κ, one obtains $2N$ eigenvalues $E_{n\kappa}$ and corresponding coefficient vectors $\mathbf{c}^{(n\kappa)}$ where $n = 1, 2, \ldots, 2N$. The first N solutions approximate the negative continuum, while the remaining N solutions approximate the bound states and the positive continuum. The main point here is that radial wave functions can be represented computationally by a set of coefficients $c(n\kappa)$. To illustrate this, let's consider second order energy shifts. It can be expressed as

$$\Delta E = \langle a|V|\delta a\rangle, \tag{70}$$

where

$$|\delta a\rangle = \sum_{n,\, \epsilon_n \neq \epsilon_a} \frac{|n\rangle\langle n|V|a\rangle}{\epsilon_n - \epsilon_a}. \tag{71}$$

When the potential V is spherically symmetric, its matrix elements are given by[6]:

$$\langle a|V|b\rangle = \int_0^\infty dr\, U(r) \left[G_{n_a\kappa_a}(r)G_{n_b\kappa_b}(r) + F_{n_a\kappa_a}(r)F_{n_b\kappa_b}(r)\right] \delta_{\kappa_a,\kappa_b}\delta_{m_a,m_b}, \tag{72}$$

which shows that the relativistic angular momentum and magnetic quantum numbers are conserved. Therefore, the state $|\delta a\rangle$ can be represented as

$$\delta\psi_{n_a\kappa_a m_a}(r) = \frac{1}{r}\begin{pmatrix} \delta G_{n_a\kappa_a}(r)\Omega_{\kappa_a m_a}(n) \\ i\delta F_{n_a\kappa_a}(r)\Omega_{-\kappa_a m_a}(n) \end{pmatrix}, \tag{73}$$

where

$$\begin{pmatrix} \delta G_{n_a\kappa_a}(r) \\ \delta F_{n_a\kappa_a}(r) \end{pmatrix} = \sum_{n,\, \epsilon_n \neq \epsilon_{n_a\kappa_a}} \frac{U_{n_a\kappa_a n\kappa_a}}{\epsilon_n - \epsilon_{n_a\kappa_a}} \begin{pmatrix} G_{n\kappa_a}(r) \\ F_{n\kappa_a}(r) \end{pmatrix}, \tag{74}$$

and

$$V_{n_a\kappa_a n\kappa_a} = \int_0^\infty dr\, U(r) \left[G_{n\kappa_a}(r)G_{n_a\kappa_a}(r) + F_{n\kappa_a}(r)F_{n_a\kappa_a}(r)\right]. \tag{75}$$

By substituting the approximation from Eq. (66) into Eq. (65) it becomes clear that the corrections to the radial wave functions correspond to corrections in their coefficients:

$$\delta c(n_a\kappa_a) = \sum_{n,\, \epsilon_n \neq \epsilon_{n_a\kappa_a}} \frac{U_{nn_a\kappa_a}}{\epsilon_n - \epsilon_{n_a\kappa_a}} c(n\kappa_a). \tag{76}$$

Thus, operations on radial wave functions can be effectively translated into operations on the coefficients that represent them.

7.2 B-splines as finite basis set

In this section a short introduction to B-splines is provided where we follow [14]. Different methods using finite basis sets vary primarily in their selection of basis functions u_i and

the way boundary conditions are applied. The choice of basis functions significantly impacts the accuracy and efficiency of numerical solutions to differential equations, such as the radial Dirac equation. We briefly discuss the approach discussed in [14, 15], where finite basis sets are constructed using B-splines, a popular choice due to their flexibility, local support, and ability to form a complete basis set over a given interval. A B-spline of order K is a piecewise polynomial function with a maximum degree of $K-1$ that is defined over a partition of the cavity interval $[0, R_{\rm cav}]$ into subintervals. The endpoints of these subintervals are specified by a sequence of knots t_i, where $i = 1, 2, \ldots, N+K$, with N being the total number of B-splines. Each B-spline function of order K, denoted by $B_{i,K}(x)$, is defined recursively in terms of the knot sequence $\{t_i\}$ as follows:

$$B_{i,1}(x) = \begin{cases} 1, & t_i \le x < t_{i+1}, \\ 0, & \text{otherwise}, \end{cases} \tag{77}$$

and

$$B_{i,K}(x) = \frac{x - t_i}{t_{i+K-1} - t_i} B_{i,K-1}(x) + \frac{t_{i+K} - x}{t_{i+K} - t_{i+1}} B_{i+1,K-1}(x). \tag{78}$$

The B-spline basis vanishes everywhere except for x in $[t_i, t_{i+K})$. Within this range, it is a piecewise polynomial of degree $K-1$ at most. The sum of all B-splines that do not vanish at a given point is always one, providing a partition of unity. An example is shown in Fig. 4. For atomic physics calculations, the choice of the knot sequence is crucial. The knots t_i are chosen such that the first multiplicity K are at $x = 0$ and the last K are at $x = R_{\rm cav}$, ensuring the desired boundary conditions are met. In finite basis set calculations, the distinct knots define a strictly increasing sequence, which effectively determines the grid resolution and affects the accuracy of the numerical solution. The choice of the order K of the B-splines and the knot distribution strategy must be carefully optimized based on the physical problem at hand and the required computational accuracy. Using the notation of [14], the basis functions u_i were chosen as:

$$u_i(r) = \begin{pmatrix} B_i(r) \\ 0 \end{pmatrix}, \quad \text{for } i = 1, \ldots, N, \tag{79}$$

and

$$u_i(r) = \begin{pmatrix} 0 \\ B_{i-N}(r) \end{pmatrix}, \quad \text{for } i = N+1, \ldots, 2N. \tag{80}$$

The MIT bag-model boundary conditions were implemented by adding boundary terms to the action in Eq. (65), which led to the conditions $G(0) = 0$ and $G(R_{\rm cav}) = F(R_{\rm cav})$. These boundary conditions effectively confine the wave functions within the cavity and eliminate the so-called spurious states, which are states that do not belong to the physical spectrum but appear due to numerical discretization and finite basis trunca-

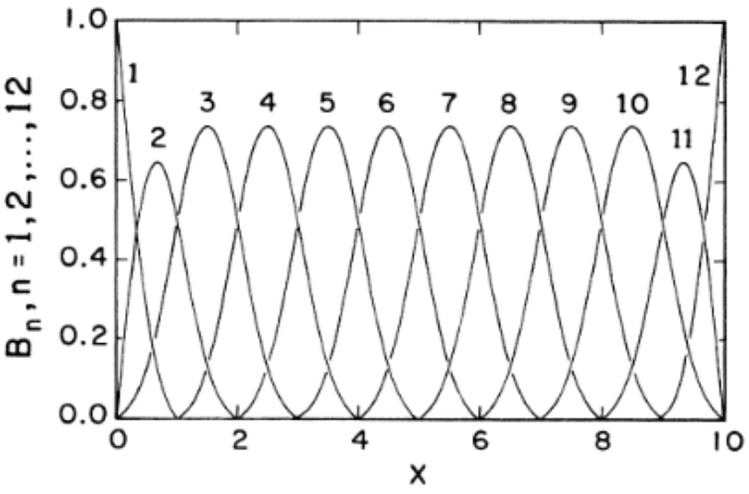

Figure 4: The twelve B splines of order k =3, $B_{i,3}(x)$, for the uniform knot sequence $t_1 = t_2 = t_3 = 0$, $t_4 = 1, t_5 = 2... = t_{12} = 9$, $t_{13} = t_{14} = t_{15} = 10$ are shown. At any point there are three non- vanishing functions that sum to 1. In our applications to the Dirac equation, the knot sequence is distributed exponentially rather than uniformly. Picture is taken from [14].

tion. Such states are generally associated with nonphysical energies, especially those in the bound-state spectrum region. A different basis choice was made in [16]:

$$u_i(r) = \begin{pmatrix} B_i(r) \\ \left(\frac{\kappa+\frac{1}{2}}{B_{i-N}(r)}\right) \end{pmatrix}, \tag{81}$$

for $i = 1, \ldots, N$, and

$$u_i(r) = \begin{pmatrix} \left(\frac{\kappa+\frac{1}{2}}{B_{i-N}(r)}\right) \\ B_{i-N}(r) \end{pmatrix}, \tag{82}$$

for $i = N+1, \ldots, 2N$. This approach assumes an extended nucleus, rather than a point-like nucleus, where the nuclear potential is softened from below. This method is referred to as the dual kinetic balance (DKB) approach [16]. The paper mentioned, argues that this choice of basis functions prevents spurious states from appearing in the numerical spectrum. For practical calculations in this thesis, the DKB approach has been adopted. In practical numerical calculations involving B-spline basis sets, it is often necessary to modify the set to satisfy specific boundary conditions. Specifically, omitting the first and last B-spline functions provides the boundary conditions at the origin for $|\kappa| = 1$. For cases where $|\kappa| > 1$, it is additionally required to remove the second B-spline function. As discussed in [16], this removal has no impact on the results, as the associated functions do not contribute significantly to the numerical solution. Similarly, removing the last two B-spline functions can be used to enforce the boundary condition $G(R_{\text{cav}}) = F(R_{\text{cav}}) = 0$. According to [16], this adjustment also does not affect the outcome, implying that the choice of B-spline functions near the boundaries is flexible without loss of accuracy. The radial wave functions $G_{n\kappa}(r)$ and $F_{n\kappa}(r)$, expressed in terms of B-spline basis functions,

are then given by the following sums [6]:

$$G_{n\kappa}(r) = \sum_{i=2}^{N-1} \left\{ \frac{c_i(n\kappa)B_i(r) + \frac{c_{N+i}(n\kappa)}{2m_e}\left[B_i'(r) - \frac{\kappa}{r}B_i(r)\right]}{1 + \frac{c_{N+i}(n\kappa)}{2m_e}} \right\}, \tag{83}$$

$$F_{n\kappa}(r) = \sum_{i=2}^{N-1} \left\{ \frac{c_i(n\kappa)B_i(r) + \frac{c_{N+i}(n\kappa)}{2m_e}\left[B_i'(r) + \frac{\kappa}{r}B_i(r)\right]}{1 + \frac{c_{N+i}(n\kappa)}{2m_e}} \right\}. \tag{84}$$

In these equations, $B_i(r)$ represents the B-spline basis functions, $B_i'(r)$ denotes their first derivative with respect to r, and $c_i(n\kappa)$ are the coefficients obtained from solving the generalized eigenvalue problem discussed earlier. By employing this B-spline basis set, we can accurately represent the radial wave functions necessary for fully relativistic calculations, such as the computation of radiative corrections. This approach ensures that the numerical solutions are stable and physically meaningful, avoiding spurious states and maintaining proper boundary conditions.

7.3 Generalized exponential integral $E_n(x)$

The generalized exponential integral, denoted as $E_n(x)$, is an important special function in mathematical physics, engineering, and applied mathematics. It arises in problems involving radiative transfer, potential theory, quantum mechanics, and many other fields where integration involving an exponential function in the integrand occurs. The generalized exponential integral is defined for a real or complex parameter n and a positive real variable x by the following integral:

$$E_n(x) = \int_1^\infty \frac{e^{-xt}}{t^n}\, dt, \quad \text{for } x > 0,\ n \in \mathbb{R}. \tag{85}$$

For the special case when $n = 1$, $E_1(x)$ is simply the exponential integral function $\mathrm{Ei}(x)$, which is often encountered in many applications. For positive integers n, the function $E_n(x)$ can be computed recursively using a relationship derived from integration by parts. This recursive formula provides a practical means for calculating $E_n(x)$ for different values of n without evaluating the integral directly. The recursive formula for the generalized exponential integral $E_n(x)$ is obtained by integrating by parts. Starting from the integral definition,

$$E_n(x) = \int_1^\infty \frac{e^{-xt}}{t^n}\, dt, \tag{86}$$

we perform integration by parts by setting $u = \frac{1}{t^n}$ and $dv = e^{-xt}\, dt$. Then, $du = -n\frac{dt}{t^{n+1}}$ and $v = -\frac{e^{-xt}}{x}$. Applying the integration by parts formula,

$$\int u\, dv = uv - \int v\, du, \tag{87}$$

we get

$$E_n(x) = \left[-\frac{e^{-xt}}{xt^n} \right]_1^\infty + \frac{n}{x} \int_1^\infty \frac{e^{-xt}}{t^{n+1}}\, dt. \tag{88}$$

Evaluating the first term at the limits, we find that the boundary term vanishes as $t \to \infty$ and is equal to $-\frac{e^{-x}}{x}$ at $t = 1$. Thus, the expression simplifies to

$$E_n(x) = \frac{e^{-x}}{x} + \frac{n}{x} E_{n+1}(x). \tag{89}$$

This is the recursive relation for $E_n(x)$ [17]:

$$E_n(x) = \frac{e^{-x}}{x} + \frac{n}{x} E_{n+1}(x). \tag{90}$$

Starting with the base case $E_1(x) = -\mathrm{Ei}(-x) = \int_x^\infty \frac{e^{-t}}{t}\, dt$, one can compute $E_2(x), E_3(x)$, and so on, using the recursive formula. For example,

$$E_2(x) = \frac{e^{-x}}{x} + \frac{1}{x} E_3(x), \tag{91}$$

and

$$E_3(x) = \frac{e^{-x}}{x} + \frac{2}{x} E_4(x). \tag{92}$$

Thus, the recursive approach provides an efficient method for computing $E_n(x)$ for higher values of n and arbitrary positive x, avoiding the need for direct integration. To fully utilize this recursive method, it is essential to accurately compute the base case $E_1(x)$. The first-order exponential integral $E_1(x)$ can be numerically computed using well-established methods depending on the value of x. When x is small (typically $x < 1$), the following series expansion is used:

$$E_1(x) = -\gamma - \ln(x) - \sum_{k=1}^{\infty} \frac{(-x)^k}{k \cdot k!}, \tag{93}$$

where γ is the Euler-Mascheroni constant. This series converges rapidly for small x, providing an accurate numerical approximation. When x is large (typically $x > 1$), the asymptotic expansion is more appropriate:

$$E_1(x) \sim \frac{e^{-x}}{x} \left(1 - \frac{1}{x} + \frac{2}{x^2} - \cdots \right). \tag{94}$$

This expansion is effective because the exponential decay dominates, and the series terms become smaller with increasing x. For values of x that are neither very small nor very large, numerical quadrature methods or continued fraction representations can be employed to ensure accuracy across a wide range. With an accurate computation of $E_1(x)$, the recursive formula in Eq. (90) can be used to compute higher order exponential integrals $E_n(x)$ efficiently. This approach is particularly useful in scenarios where high

precision is required for various n and x values, providing a robust framework for evaluating these integrals without resorting to complex or time-consuming numerical integration techniques.

7.4 Calculation of leptonic Uehling potential

Another representation for the before discussed,theoretically well understood, leptonic Uehling potential being way more useful for actual computations is the following [18]:

$$V_p(r) = -\frac{2\alpha Z\alpha}{3}\frac{1}{r}\int_0^\infty r'\rho(r')dr'[\chi_2(2|r-r'|) - \chi_2(r+r'|)], \tag{95}$$

with the charge density normalization $4\pi\int_0^\infty drr^2\rho(r) = 1$. $\chi_2(z)$ belongs to a family of functions defined like this

$$\chi_n(z) = \int_1^\infty dte^{-}tzt^{-n}\left(1+\frac{1}{2t^2}\right)\left(1-\frac{1}{t^2}\right)^{1/2}. \tag{96}$$

Using these expressions to describe the uehling potential we can study different limits. Lets first discuss the limit of V_p as $r \to 0$:

$$V_p(0) = -\frac{8\alpha Z\alpha}{3}\int_0^\infty dr'r'\rho(r')\chi_1(2r'). \tag{97}$$

For very large distances from the nucleus we can expand in moments of the nuclear charge distribution where $\langle r^{2n}\rangle = 4\pi\int_0^\infty drr^{2n+2}\rho(r)$. We therefore get [19]:

$$V_p(r) = -\frac{2\alpha Z\alpha}{3\pi}\times\frac{1}{r}[\chi_1(2r) + \frac{2}{3}\langle r^2\rangle\chi_{-1}(2r) + \frac{2}{15}\langle r^4\rangle\chi_{-3}(2r) + ...]. \tag{98}$$

Trivially here the first term denotes the point nucleus uehling potential scaling like $\frac{\alpha}{\pi}$. If we assume a uniform charge density with radius R Eq. (95) can be cast into the following expression after carrying out the radial integration first.

$$V_p(r) = -\frac{\alpha Z\alpha}{2\pi R^3}\frac{1}{r}\left[\frac{2}{5}r + \varphi(2(R+r)) - \varphi(2(R-r))\right], \tag{99}$$

for $r \leq R$ and for $r > R$

$$V_p(r) = -\frac{\alpha Z\alpha}{2\pi R^3}\frac{1}{r}\left[\frac{2}{5}r + \varphi(2(R+r)) - \varphi(2(r-R)) + R\chi_3(2(r-R))\right], \tag{100}$$

with $\varphi(z) = \frac{1}{2}R\chi_3(z) + \frac{1}{4}\chi_4(z)$.
Analogously for Eq. (97) we find the expression

$$V_p(0) = -\frac{\alpha Z\alpha}{\pi R^3}\left[\frac{1}{5} - R\chi_2(2R) - \frac{1}{2}\chi_3(2R)\right]. \tag{101}$$

The structure of the functions $\chi_n(z)$ can be described by the well known Bessel functions $Ki(z)$. Here we find after the substitution $t = cosh(u)$ the following relation

$$\chi_n(z) = Ki_{n-1}(z) - \frac{1}{2}Ki_{n=1}(z) - \frac{1}{2}Ki_{n+3}(z). \tag{102}$$

For $Ki_p(z)$ with p being positive we can further decompose these into modified Bessel functions $K_0(z), K_1(z)$ and $Ki_1(z)$ where the latter is related like:

$$Ki_1(z) = \int_z^\infty dx K_0(x), \tag{103}$$

$$Ki_1(0) = \frac{\pi}{2}. \tag{104}$$

Negative integer $p = -m$ can be treated with the following relation:

$$Ki_{-m}(z) = \left(-\frac{d}{dz}\right)^m K_0(z). \tag{105}$$

This means for $n \leq -3$, $\chi_n(z)$ can be described solely using the modified Bessel functions. If once $\chi_n(z)$ is calculated one automatically has all solutions for functions with lower n by differentiating.

$$\chi_{n-1}(z) = -\frac{d\chi_n(z)}{dz}. \tag{106}$$

So we only need to calculate $\chi_4(z)$ and iterate for lower integer to carry out the calculations containing $\chi_n(z)$ in the above equations.

8 Hadronic vacuum polarization energy shift

8.1 Analytical point like nucleus

After an introduction to the solutions of the radial dirac equation in section 3 and the derivation of the hadronic Uehling potential we are now able to calculate energy shifts duo to hadronic vacuum polarization for elctronic and muonic systems. Generally the uehling potential leads to a shift of atomic energy levels which for the leading order term is given by:

$$\Delta E_{n\kappa m} = \langle n\kappa m|\delta V|n\kappa m\rangle = \int_0^\infty dr\, \delta V(r) \left[g^2_{n\kappa}(r) + f^2_{n\kappa}(r)\right] r^2 \tag{107}$$

Hence the energy shift for the 1s state, considering a pointlike nucleus, is given by the first order pertubation like this:

$$\Delta E^{\text{analytical}}_{\text{point}}(1s) = \langle 1s|\delta V^{\text{approx}}_{\text{point}}(r)|1s\rangle = \int_0^\infty dr\ \left(g^2(r)+f^2(r)\right) r^2 \delta V^{\text{approx}}_{\text{point}}(r) \tag{108}$$

$$\Delta E^{\text{approx}}_{\text{point}}(1s) = \frac{2\lambda}{\Gamma(2\gamma+1)} \int_0^\infty dr\, (2\lambda r)^{2\gamma} e^{-2\lambda r} \delta V^{\text{approx}}_{\text{point}}(r) \tag{109}$$

with the analytical expressions for the radial wave functions [5]:

$$\left.\begin{matrix} g(r) \\ f(r) \end{matrix}\right\} = \pm\sqrt{2}\lambda^{3/2} \left(\frac{(m\pm E)(Z\alpha m+\lambda)}{\Gamma(2\gamma+1)Z\alpha m^2}\right)^{1/2} e^{-\lambda r}(2\lambda r)^{\gamma-1} \tag{110}$$

$$\lambda = Z\alpha m_e, \quad \gamma = \sqrt{1-(Z\alpha)^2} \tag{111}$$

and the approximated parametrized pointlike potential $V^{\text{approx}}_{\text{point}}(r)$:

$$\delta V^{\text{approx}}_{\text{point}}(r) = -\frac{2Z\alpha}{r} B_1 E_1\left(\frac{r}{\sqrt{C_1}}\right), \tag{112}$$

we find the following expression for the energy shift by continuosly follwoing the derivation of [20]:

$$\Delta E^{\text{analytical}}_{\text{point}}(1s) = -\frac{Z\alpha\lambda(2\lambda\sqrt{C_1})^{2\gamma}B_1}{\gamma^2} {}_2F_1\left(2\gamma, 2\gamma; 1+2\gamma; -2\lambda\sqrt{C_1}\right). \tag{113}$$

with the hypergeometric function ${}_2F_1(a,b;c;x)$ defined as:

$${}_2F_1(a,b;c;x) = \sum_{n=0}^{\infty} \frac{a_n b_n x^n}{c_n\, n!}. \tag{114}$$

An expansion in orders of $(Z\alpha)$ can be made by taylor expanding the sinc function appearing duo to the spherically symmetric potential. Up to order $(Z\alpha)^6$ it is given by [10]:

$$\begin{aligned} \Delta E^{\text{analytical}}_{\text{point}}(1s) = &-4B_1C_1m_e^3(Z\alpha)^4 \\ &+ \frac{32B_1C_1^{3/2}m_e^4(Z\alpha)^5}{3} \\ &- 4B_1C_1m_e^3(Z\alpha)^6 \\ &\times \left[1+6C_1m_e^2 - \ln(2Z\alpha\sqrt{C_1}m_e)\right] \\ &+ \cdots . \end{aligned} \tag{115}$$

(13)

Following the same approach the 2s state Expansion is given by[10]:

$$\Delta E^{\text{analytical}}_{\text{point}}(2s) = -\frac{1}{2}B_1C_1m_e^3(Z\alpha)^4 + \frac{4B_1C_1^{3/2}m_e^4(Z\alpha)^5}{3} + \cdots . \tag{116}$$

In both of these expansions around $Z\alpha$ the lowest order term represents the non relativistic and pointlike value for the energy shift:

$$\Delta E^{\text{analytical}}_{\text{nonrel.,point}}(1s) = -4B_1C_1m_e^3(Z\alpha)^4, \tag{117}$$

$$\Delta E^{\text{analytical}}_{\text{nonrel.,point}}(2s) = -\frac{1}{2}B_1C_1m_e^3(Z\alpha)^4. \tag{118}$$

8.2 Approximate finite size energy shift for hadronic VP

The hadronic energy shift for an extended nucleus was numerically computed due to the lack of an analytical solution. This approach involves solving the Dirac equation with the potentials for an extended nucleus included. The computation is performed using a B-spline representation we introduced earlier. Here operations on radial wave functions can be effectively translated into operations on the coefficients that represent them. This finally allows for the extraction of the corresponding energy eigenvalues. In [6], non-perturbative, all-order numerical results has been provided for the exact wave functions induced by the hadronic Uehling potential. He developed a computer code that approximates the real wave function using a spline representation. This method enables the calculation of the energy shift through the following integral numerically in Fortran.

$$\Delta E^{\text{approx}}_{\text{fns}} = \int_0^\infty dr\, \delta V^{\text{approx}}_{\text{fns}}(r) \left[g^2_{n\kappa}(r) + f^2_{n\kappa}(r)\right] r^2 \tag{119}$$

with $\delta V^{\text{approx}}_{\text{fns}}(r)$ defined in Eq. (56) where the parametrization was approximated by choosing only the first energy domain up to infinity.

9 Results

In the following we will use the analytical point like hadronic energy shift $\Delta E^{\text{analytical}}_{\text{point}}$ as well as the nonrelatitvistic energy shift $\Delta E^{\text{analytical}}_{\text{nonrel.,point}}$ as refenerence for the values we obtain considering an finite nucelar size. The results for diferent Z are given in table 2 where for R_{rms} we used [10, 21]. In table 3 we also calculated the mentioned approach for the $2s, 2p_{1/2}$ and $2p_{3/2}$ exited states of the considered hydrogenic systems. The non-relativistic results for $Z = 1$ are in good agreement with other methods within the estimated error margins found in [10]. However, as Z increases, the discrepancy between non-relativistic and relativistic results becomes more pronounced, reaching up to an order of magnitude difference for high Z. This indicates that a relativistic approach is necessary for all ions considered, except for hydrogen. Furthermore, results obtained using first-order perturbation theory with analytical Dirac-Coulomb wave functions align with those derived from the exact wave function of the hadronic Uehling potential for a finite nucleus only for low Z. For high Z, finite nuclear size effects become significant and exact calculations show considerable deviation from the first-order perturbative results. This

highlights the limitations of the perturbative approach, particularly for heavy elements like lead. In table 4 and 5 we show the total lamb shift ΔE_{LS} for the $1s$ ground state and the exited states $2s, 2p_{1/2}$ and $2p_{3/2}$. The theoretical values for the Lamb shift, along with their uncertainties shown in tables, reveal that the current uncertainties related to the nuclear charge distribution are too large to make the hadronic vacuum polarization (VP) observable. Specifically, these uncertainties need to be reduced by at least an order of magnitude [10]. Additionally, quantum electrodynamics (QED) corrections, which are crucial for accurately determining the Lamb shift, need to be calculated with higher precision. Without these improvements in both nuclear charge distribution models and QED calculations, it will remain difficult to detect the small effects of hadronic VP. This is the exact reason why it is of interest to consider muonic systems as well. In table 6 and 7 we display the values of hadronic polarization energy shifts for the muonic systems H, Zr, Sn and Pb. Since the before discussed effect of the muon being much more sensetive to finite nuclear size corrections we only state the numerical results and the nonrelatvistic as the relativistic point like energy shifts differ strongly as Z increases. Only for muonic hydrogen these values are of comparable accuracy [10]. We emphasize that, unlike the approach in [10], our calculation of the parameterized hadronic Uehling potential only includes contributions from the first energy region, extending up to infinity. This approximation is valid for electronic systems up to $Z = 96$. However, for muonic systems, discrepancies begin to appear as early as $Z = 1$, which explains the variations in our results for muonic hydrogen compared to those in [10]. Still for muonic hydrogen agreement in the numbers is found considering the given uncertainties provided in the other paper. For muonic Zr, Sn, and Pb, we compare our corrections to the muonic binding energies with those listed in table 8 taken from [22, 23, 24]. We have to notice only ^{112}Sn got references while we worked with ^{120}Sn. It is important to note that the effect of muonic vacuum polarization contributes nearly twice as much to the energy shift as hadronic vacuum polarization. As a result, our calculated values for higher Z muonic systems show good agreement with the reference results. Additionally, we observe a sign reversal in the binding energy corrections. This can be attributed to the fact that, in this work, we account for corrections to the Dirac energy, which was not the focus in the previous studies.

10 Summery and Outlook

This study addressed the challenges of incorporating hadronic vacuum polarization (HVP) into theoretical models of atomic energy levels, with a focus on hydrogen-like ions and muonic atoms. While quantum electrodynamics (QED) remains one of the most precise theories in physics, the need to account for more subtle quantum effects is crucial as experimental techniques advance. By utilizing a semiempirical approach, this research constructed a hadronic polarization function based on experimental electron-positron an-

nihilation data and develops an effective relativistic Uehling potential. The study employs analytical Dirac-Coulomb wave functions and accounts for finite nuclear size effects to quantify energy corrections due to HVP. This method provides a more accurate representation of HVP impacts, particularly in the context of muonic systems, which offer enhanced sensitivity to such effects due to the muon's greater mass and closer proximity to the nucleus. Here the pointlike nucleus and nonrelativistic approach fails completely. Especially for muonic systems it could be of interest to include more energy regions to calculate the hadronic vacuum polarization energy shift even more precisely. Future work is planned to focus directly on calculating these energy corrections to higher precison for a rnge of muonic systems. This is motivated by considering current experimental uncertainties for transition energies. As we can see for example considering muonic lead in [22], those uncertainties for low energy level transitions are around 100 eV. For this reason energy shifts duo to hadronic vacuum polarization are not observable at current level of accuarcy. The primary source of uncertainty in these calculations arises from the nuclear model used. This uncertainty can be mitigated by adopting more sophisticated charge distribution models. Using the Fermi distribution model and accounting for recoil effects allows for improved accuracy in theoretical predictions by providing a more realistic description of the nuclear charge distribution compared to simpler models. This can help reduce uncertainties in calculations related to hadronic vacuum polarization and other nuclear effects [25]. In conclusion, while significant progress has been made in understanding and accounting for nuclear polarization effects, there remains a compelling need for ongoing refinement in this area. The pursuit of greater accuracy in nuclear polarization not only enhances the precision of theoretical models but also drives advancements in experimental techniques and our overall understanding of fundamental physics. As we continue to push the boundaries of precision measurement, addressing the subtle complexities of nuclear polarization effects will be crucial for unraveling the nuances of quantum electrodynamics and exploring potential new physics beyond the Standard Model. By striving for improved models and more accurate calculations, we pave the way for deeper insights into the fabric of the universe, ultimately contributing to the advancement of science and our comprehension of the fundamental forces that govern our world.

Z	R_{rms} (fm)	$\Delta E^{\mathrm{analytical}}_{\mathrm{nonrel.,\ point}}$ (eV)	$\Delta E^{\mathrm{analytical}}_{\mathrm{rel.,\ point}}$ (eV)	$\Delta E^{\mathrm{approx}}_{\mathrm{rel.,\ fns}}$ (eV)
1	0.8783(86)	-1.3953[-11]	-1.3963[-11]	-1.3961[-11]
14	3.1224(24)	-5.3605[-7]	-5.9178[-7]	-5.7561[-7]
20	3.4776(19)	-2.2326[-6]	-2.7133[-6]	-2.5596[-6]
36	4.1884(22)	-2.3437[-5]	-4.2698[-5]	-3.4847[-5]
40	4.2694(10)	-3.5722[-5]	-7.4499[-5]	-5.7795[-5]
50	4.6519(21)	-8.7211[-5]	-2.7132[-4]	-1.7880[-4]
54	4.7859(48)	-1.1865[-4]	-4.4452[-4]	-2.7062[-4]
74	5.3658(23)	-4.1843[-4]	-5.0982[-3]	-1.8010[-3]
82	5.5012(13)	-6.3088[-4]	-1.4127[-2]	-3.6929[-3]

Table 2: Hadronic vacuum polarization energy shifts calculated with different formulas for the 1s ground state of hydrogenic systems: $\Delta E^{\mathrm{analytical}}_{\mathrm{nonrel.,\ point}}$ being the nonrelativistic expansion term,$\Delta E^{\mathrm{analytical}}_{\mathrm{rel.,\ point}}$ is the energy shift for analytic radial wave functions and a point like nucleus,$\Delta E^{\mathrm{approx}}_{\mathrm{rel.,\ fns}}$ is the shift while considering full numerical calculated FNS radial wave functions using B Splines with the approximated parametrized hadronic uehling potential inserted.

Z	$\Delta E^{\mathrm{approx}}_{\mathrm{rel.,\ fns}}(2s)$ (eV)	$\Delta E^{\mathrm{approx}}_{\mathrm{rel.,\ fns}}(2p_{1/2})$ (eV)	$\Delta E^{\mathrm{approx}}_{\mathrm{rel.,\ fns}}(2p_{3/2})$ (eV)
1	-1.7452[-12]	-1.7427[-17]	-6.4268[-23]
14	-7.2616[-8]	-1.4314[-10]	-4.1679[-15]
20	-3.2603[-7]	-1.3206[-9]	-4.5345[-14]
36	-4.6305[-6]	-6.2614[-8]	-2.6017[-12]
40	-7.7918[-6]	-1.3141[-7]	-5.3580[-12]
50	-2.5167[-5]	-6.8424[-7]	-2.8065[-11]
54	-3.8865[-5]	-1.2509[-6]	-5.0359[-11]
74	-2.9322[-4]	-1.9574[-5]	-6.2174[-10]
82	-6.4027[-4]	-5.5407[-5]	-1.4616[-9]

Table 3: Hadronic energy shifts calculated by solving the Dirac equation, with inclusion of the potentials for an extended nucleus, using a B-spline representation and extracting the corresponding energy eigenvalues for $2s$, $2p_{1/2}$, and $2p_{3/2}$ states for different Z values.

Z	$\Delta E_{\mathrm{LS}}(1s)$ (eV)	$\Delta E_{\mathrm{LS}}(2s)$ (eV)
1	3.8000262(7)(57)[-5]	4.3218005(8)(72)[-6]
14	4.80447(18)(4)[-1]	6.40329(23)(5)[-2]
20	1.63263(6)(2)[0]	2.21409(9)(2)[-1]
36	1.18259(16)(3)[1]	1.68814(25)(4)[0]
54	4.6920(18)(6)[1]	7.1723(27)(9)[0]
74	1.5422(13)(2)[2]	2.5876(20)(4)[1]
82	2.4440(26)(3)[2]	4.2924(44)(4)[1]

Table 4: Lamb shifts for the $1s$ and $2s$ states for various Z values. Errors are denoted in parentheses, where the second one is due to the error of the nuclear charge radius, and the first one is due to all other errors of individual theoretical contributions added quadratically. Taken from [10, 26].

Z	$\Delta E_{\mathrm{LS}}(2p_{1/2})$ (eV)	$\Delta E_{\mathrm{LS}}(2p_{3/2})$ (eV)
1	-5.30919(4)(0)[-8]	5.177459[-8]
14	-1.7316(4)(0)[-3]	2.1808(4)(0)[-3]
20	-6.2940(35)(0)[-3]	9.6566(34)(0)[-3]
36	-3.4426(62)(1)[-2]	1.2089(9)(0)[-1]
54	6.0317(72)(36)[-1]	7.413(10)(0)[-1]
74	1.6390(33)(3)[0]	3.1615(30)(0)[0]
82	3.9045(72)(4)[0]	5.1088(57)(0)[0]

Table 5: Lamb shifts for the $2p_{1/2}$ and $2p_{3/2}$ states for various Z values. Errors are denoted in parentheses, where the second one is due to the error of the nuclear charge radius, and the first one is due to all other errors of individual theoretical contributions added quadratically. Taken from [10, 26].

Z	$\Delta E^{\mathrm{approx}}_{\mathrm{rel.,\ fns}}(1s)$ (eV)	$\Delta E^{\mathrm{approx}}_{\mathrm{rel.,\ fns}}(2s)$ (eV)
1	-1.2212[-4]	-1.5266[-5]
40	-52.8315	-7.6611
50	-79.0317	-12.0171
82	-157.0541	-26.5259

Table 6: Hadronic vacuum polarization energy shifts of different muonic systems for the $1s$ and $2s$ states.

Z	$\Delta E^{\mathrm{approx}}_{\mathrm{rel.,\ fns}}(2p_{1/2})$ (eV)	$\Delta E^{\mathrm{approx}}_{\mathrm{rel.,\ fns}}(2p_{3/2})$ (eV)
1	-1.7764[-10]	-2.4150[-11]
40	-1.1194	-0.7182
50	-3.6105	-2.4254
82	-29.7168	-22.5823

Table 7: Hadronic vacuum polarization energy shifts of different muonic systems for the $2p_{1/2}$ and $2p_{3/2}$ states.

State	^{208}Pb	^{120}Zr	^{112}Sn
$1s_{1/2}$	0.410	0.137	0.211
$2s_{1/2}$	0.071	0.020	-
$2p_{1/2}$	0.074	0.003	0.009
$2p_{3/2}$	0.056	0.002	0.006

Table 8: Correction to muonic binding energy duo to muonic and hadronic vacuum polarization in (keV). Posititve corrections resemble an increase in binding energy. Numbers are taken from [14, 23].

References

[1] S. Sturm et al. "g Factor of Hydrogenlike $^{28}Si^{13+}$". In: *Phys. Rev. Lett.* 107 (2 July 2011), p. 023002. DOI: 10.1103/PhysRevLett.107.023002. URL: https://link.aps.org/doi/10.1103/PhysRevLett.107.023002.

[2] E. Borie and G. A. Rinker. "The energy levels of muonic atoms". In: *Rev. Mod. Phys.* 54 (1 Jan. 1982), pp. 67–118. DOI: 10.1103/RevModPhys.54.67. URL: https://link.aps.org/doi/10.1103/RevModPhys.54.67.

[3] A. Antognini et al. "Proton Structure from the Measurement of 2S-2P Transition Frequencies of Muonic Hydrogen". In: *Science* 339.6118 (2013), pp. 417–420. DOI: 10.1126/science.1230016. eprint: https://www.science.org/doi/pdf/10.1126/science.1230016. URL: https://www.science.org/doi/abs/10.1126/science.1230016.

[4] URL: https://physics.nist.gov/cuu/pdf/wall_2018.pdf.

[5] W. Greiner. *Theoretische Physik Band 6: Relativistische Quantenmechanik – Wellengleichungen*. Verlag Harri Deutsch, Thun und Frankfurt am Main, 1987.

[6] H. Çakır. "Quantum Electrodynamic Theory of Few-Electron Highly Charged Ions". PhD thesis. University Heidelberg, Jan. 2020.

[7] F. Jegerlehner. "Hadronic contributions to the photon vacuum polarization and their role in precision physics". In: *Journal of Physics G: Nuclear and Particle Physics* 29.1 (Dec. 2002), pp. 101–110. ISSN: 0954-3899. DOI: 10.1088/0954-3899/29/1/311. URL: http://dx.doi.org/10.1088/0954-3899/29/1/311.

[8] S. Breidenbach. "Hadronic vacuum polarization in atoms". Bachelor Thesis. Ruprecht-Karls-Universität, Heidelberg, 2018. URL: https://hdl.handle.net/21.11116/0000-0001-0229-F.

[9] W. Greiner and J. Reinhardt. *Quantenelecktrodynamik*. Verlag Harri Deutsch, Thun und Frankfurt am Main, 1984.

[10] S. Breidenbach et al. "Hadronic vacuum polarization correction to atomic energy levels". In: *Phys. Rev. A* 106 (4 Oct. 2022), p. 042805. DOI: 10.1103/PhysRevA.106.042805. URL: https://link.aps.org/doi/10.1103/PhysRevA.106.042805.

[11] H. Burkhardt et al. “Uncertainties in the Hadronic Contribution to the QED Vacuum Polarization”. In: *Z. Phys. C* 43 (1989), pp. 497–501. DOI: 10.1007/BF01506546.

[12] T. Weigand. *Lecture notes for Quantum Field Theory I + II*. Unpublished lecture notes. 2014.

[13] H. Burkhardt and B. Pietrzyk. “Update of the hadronic contribution to the QED vacuum polarization”. In: *Physics Letters B* 513.1 (2001), pp. 46–52. ISSN: 0370-2693. DOI: https://doi.org/10.1016/S0370-2693(01)00393-8. URL: https://www.sciencedirect.com/science/article/pii/S0370269301003938.

[14] W. R. Johnson, S. A. Blundell, and J. Sapirstein. “Finite basis sets for the Dirac equation constructed from B splines”. In: *Phys. Rev. A* 37 (2 Jan. 1988), pp. 307–315. DOI: 10.1103/PhysRevA.37.307. URL: https://link.aps.org/doi/10.1103/PhysRevA.37.307.

[15] H. Bachau et al. “Applications of B-splines in atomic and molecular physics”. In: *Reports on Progress in Physics* 64.12 (Nov. 2001), p. 1815. DOI: 10.1088/0034-4885/64/12/205. URL: https://dx.doi.org/10.1088/0034-4885/64/12/205.

[16] V. M. Shabaev et al. “Dual Kinetic Balance Approach to Basis-Set Expansions for the Dirac Equation”. In: *Phys. Rev. Lett.* 93 (13 Sept. 2004), p. 130405. DOI: 10.1103/PhysRevLett.93.130405. URL: https://link.aps.org/doi/10.1103/PhysRevLett.93.130405.

[17] NIST. *Digital Library of Mathematical Functions - Generalized Exponential Integral*. Accessed: 2024-09-08. 2024. URL: https://dlmf.nist.gov/.

[18] L. Wayne Fullerton and G. A. Rinker. “Accurate and efficient methods for the evaluation of vacuum-polarization potentials of order $Z\alpha$ and $Z\alpha^2$”. In: *Phys. Rev. A* 13 (3 Mar. 1976), pp. 1283–1287. DOI: 10.1103/PhysRevA.13.1283. URL: https://link.aps.org/doi/10.1103/PhysRevA.13.1283.

[19] T. Franosch and G. Soff. “The influence of the nuclear shape and of the muonic vacuum polarization on strongly bound electrons”. In: *Zeitschrift für Physik D Atoms, Molecules and Clusters* 18 (1991), pp. 219–222. DOI: 10.1007/BF01437074. URL: https://doi.org/10.1007/BF01437074.

[20] E. Dizer. “Analytic Evaluation of Quantum Electrodynamic Corrections in One-Electron Ions”. Bachelor Thesis. Ruprecht-Karls-Universität, Heidelberg, 2020. URL: https://hdl.handle.net/21.11116/0000-0006-B165-0.

[21] I. Angeli and K. P. Marinova. “Table of experimental nuclear ground state charge radii: An update”. In: *Atomic Data and Nuclear Data Tables* 99.1 (2013), pp. 69–95. ISSN: 0092-640X. DOI: https://doi.org/10.1016/j.adt.2011.12.006. URL: https://www.sciencedirect.com/science/article/pii/S0092640X12000265.

[22] P. Bergem et al. “Nuclear polarization and charge moments of ^{208}Pb from muonic x rays”. In: *Phys. Rev. C* 37 (6 June 1988), pp. 2821–2833. DOI: 10.1103/PhysRevC.37.2821. URL: https://link.aps.org/doi/10.1103/PhysRevC.37.2821.

[23] T. Q. Phan et al. “Nuclear polarization in muonic ^{90}Zr”. In: *Phys. Rev. C* 32 (2 Aug. 1985), pp. 609–619. DOI: 10.1103/PhysRevC.32.609. URL: https://link.aps.org/doi/10.1103/PhysRevC.32.609.

[24] C. Piller et al. “Nuclear charge radii of the tin isotopes from muonic atoms”. In: *Phys. Rev. C* 42 (1 July 1990), pp. 182–189. DOI: 10.1103/PhysRevC.42.182. URL: https://link.aps.org/doi/10.1103/PhysRevC.42.182.

[25] I. A. Valuev et al. “Skyrme-type nuclear interaction as a tool for calculating the finite-nuclear-size correction to atomic energy levels and the bound-electron g factor”. In: *Phys. Rev. A* 101 (6 June 2020), p. 062502. DOI: 10.1103/PhysRevA.101.062502. URL: https://link.aps.org/doi/10.1103/PhysRevA.101.062502.

[26] V. A. Yerokhin and V. M. Shabaev. “Lamb shift of n = 1 and n = 2 states of hydrogen-like atoms, $1 \leq Z \leq 110$”. In: *Journal of Physical and Chemical Reference Data* 44.3 (2015).

[27] E. M. Rose. *Relativistische Elektronen-Theorie, volume I.* Hochschultaschebücher-Verlag, Mannheim Wien Zürich, 1971.

[28] E. M. Lifshitz V. B. Berestetskii and L. P. Pitaevskii. *Quantum Electrodynamics.* Pergamon Press, Oxford, UK, 1982.

[29] H. Cakir et al. “QED corrections to the g factor of Li- and B-like ions”. In: *Phys. Rev. A* 101 (6 June 2020), p. 062513. DOI: 10.1103/PhysRevA.101.062513. URL: https://link.aps.org/doi/10.1103/PhysRevA.101.062513.

Acknowledgement

First of all, I would like to thank my supervisor, Natalia Oreshkina, for her time and always giving me useful advice. Her great teaching and patience contributed a lot in improving this thesis. Also I want to thank Halil Cahir, providing a lot of useful code, and all people who proofread the final version of the thesis. At the end I would like to thank the Max Planck Institute for Nuclear Physics and especially the Theory Devison from Honorarprofessor Dr. Christoph H. Keitel for the hospitality during my work on the thesis.